https://doi.org/10.5194/egusphere-2026-825
Preprint. Discussion started: 1 June 2026


# Lidar probe volume averaging effect on the along-wind turbulence statistics

Sinem Uluocak[1,2], Andreas Rott[1,2], Alfredo Peña[3], and Martin Kühn[1,2]

[1]Carl von Ossietzky Universität Oldenburg, School of Mathematics and Science, Institute of Physics
[2]ForWind - Center for Wind Energy Research, Küpkersweg 70, 26129 Oldenburg, Germany
[3]DTU Wind and Energy Systems, Technical University of Denmark, 4000 Roskilde, Denmark

**Correspondence:** Sinem Uluocak (sinem.uluocak.dincer@uol.de)

**Abstract.** Wind lidars are increasingly used for wind turbine power estimation, load analysis, and control purposes, but their ability to accurately capture turbulence is limited by the large probe volumes of lidars, which attenuate measured turbulence through spatial averaging. We investigate the effects of probe volume averaging on lidar turbulence characteristics as a function of the probe volume over integral length scale ratios using a wind tunnel study. This is facilitated by generating tailor-made turbulent flow conditions using an active grid and by adjusting the focus distance of a short-range continuous-wave (CW) lidar. A hot-wire anemometer is used as reference sensor. First, a spectrum model for the lidar averaging effect is implemented by applying a Lorentzian filter to Mann-model spectra derived from hot-wire measurements, accurately capturing velocity spectrum attenuation with increasing probe volume averaging. Second, the ability of the lidar to estimate turbulence statistics including the integral length scale and velocity variance is evaluated by comparing lidar to hot-wire ratios across all cases. Results show that conventional lidar-derived length scales are overestimated while velocity variances are underestimated with increasing probe volume averaging. Both the modelled and conventionally derived lidar velocity variance are attenuated from 10 % to 80 % with increasing probe volume averaging. In contrast, the spectrum-based lidar variance, derived directly from the averaged lidar Doppler spectrum compensates for probe volume averaging, yielding variance estimates that are significantly less affected by this ratio with an average relative error of +20 % compared to the hot-wire data. The correction for velocity gradients in the wind tunnel flow reduces the average relative error of spectrum-based lidar velocity variances to +10 %.

## 1 Introduction

Accurate measurement of key turbulence characteristics is essential for many wind energy applications, including wind resource assessment, power-performance analysis, turbine fatigue load estimation, yaw alignment, and advanced turbine control strategies. In the atmospheric boundary layer (ABL), the most relevant parameters are typically the longitudinal i.e. along-wind turbulence intensity (TI), velocity variance, and, to a lesser extent, spectral shape and integral length scale. Traditionally, these parameters have been measured using meteorological masts equipped with in situ sensors. While these systems provide

https://doi.org/10.5194/egusphere-2026-825
Preprint. Discussion started: 1 June 2026


high-quality data, their fixed spatial position limits their ability to capture spatial variability of the flow, especially in complex terrain or near wind farms. Furthermore, mast installation is costly and often impractical for large-scale wind turbine flow measurements and in offshore conditions.

Wind lidars offer a compelling alternative as non-intrusive, remote-sensing instruments capable of measuring wind velocity along their beam with accuracy comparable to conventional meteorological masts. They can be continuous-wave (CW) or pulsed, with short-range systems operating from metres to hundreds of metres and long-range systems measuring up to tens of kilometres. Various scanning strategies such as singe-beam scans of Vertical Azimuthal Display (VAD) and Doppler Beam Swinging (DBS), or multi-beam WindScanners enable high resolution spatial mapping of the wind field. However, they are not widely accepted by wind energy standards for turbulence estimation primarily due to probe volume averaging and contamination of turbulent flow components when the lidar beam is not aligned with the target velocity component. Systematic errors can reach up to 90 % for vertical velocity variance and 70 % for horizontal velocity variance (Sathe et al., 2011).

Probe volume averaging is defined as the attenuation of turbulence scales smaller than the probe volume length of the lidar (Frehlich, 1997). In pulsed lidars, the probe volume length i.e. full width at half maximum of the probe volume typically ranges from 30 m to 100 m (Liu et al., 2019), while in CW lidars, it quadratically increases with focus distance, varying from centimetres to tens or a hundred of metres depending on the selected focus distance (van Dooren et al., 2022).

Many studies have examined the impact of probe volume averaging on the turbulent spectra of radial, also known as line-of-sight, velocities of the lidar (Drobinski et al., 2000). Most of these studies have focused on measurements taken in atmospheric conditions characterised by small turbulence scales, which suffer from large spatial filtering effects (Frehlich et al., 2008). The filtering effect due to probe volume can be readily identified from the attenuation of the turbulence spectrum of the lidar compared with that of reference sensors in the field (Sjöholm et al., 2009) and in a wind tunnel (van Dooren et al., 2022). The deviation of the lidar spectrum from that of the reference sensor appears in the high frequency range where small-scale fluctuations occur. The attenuation observed in lidar velocity spectra can be modelled and corrected by applying a spectral tensor model of atmospheric turbulence, together with a theoretical filtering function for the lidar (Frehlich et al., 1998; Mann et al., 2009; Cheynet et al., 2017; Puccioni and Iungo, 2021). In (Brugger et al., 2016), despite the reduction in systematic errors after correction, the results have a remaining systematic error of 36 % for radial velocity variance and 28 % for outer scale of turbulence which still leads to an underestimation of the radial velocity variance and an overestimation of the outer scale of turbulence. The fact that spectral tensor models are typically derived from sonic anemometer measurements at the site highlights the need for reference measurements to enable accurate lidar attenuation correction.

An alternative approach which is applicable in continuous-wave (CW) lidars, avoids the need for correction of turbulence measurements using several raw Doppler spectra to compensate for probe volume averaging and to obtain so-called 'unfiltered' turbulent statistics (Mann et al., 2010). It computes the radial velocity variance from the raw lidar Doppler spectra instead of using the time series statistics of reconstructed radial velocities. It uses the information about the flow fluctuations which is present in individual lidar Doppler spectra. Therefore, the ensemble-averaged Doppler radial velocity spectrum can be assumed as the probability density distribution of radial velocities along the probe volume. With this assumption, the radial velocity variance can be calculated from the second order moment of the averaged lidar Doppler spectrum. The correspondence

https://doi.org/10.5194/egusphere-2026-825
Preprint. Discussion started: 1 June 2026


between the ensemble-averaged Doppler spectrum and the probability density function of the radial velocities has been shown experimentally in wind tunnel and field campaigns (Branlard et al., 2013; Fu et al., 2022). Using the same method, the bias between the 'unfiltered' radial velocity variance from a nacelle lidar and that derived from a cup anemometer on a meteorological mast was found to be only 2 % (Peña et al., 2017). Wake turbulence behind a 27 m diameter test turbine was measured in (Conti et al., 2021) using a nacelle-based CW SpinnerLidar located 2.5 $D$ downstream. Turbulence enhancement near the rotor tips were quantified using the 'unfiltered' variance of the streamwise velocity. In (Fu et al., 2023), the six components of the Reynolds stress tensor were estimated using 'unfiltered' turbulence statistics obtained from nacelle-based lidar measurements. The nacelle-based lidar results showed a high agreement with those from sonic anemometer measurements, but were biased either positively or negatively for different components. Relative error of the lidar-derived along-wind variance to the one from the sonic anemometer was found to be approximately -5.5 % for the six-beam and multiple-beam nacelle lidar. A recent study introduced a method for the estimation of pulsed lidar turbulent statistics using the averaged lidar Doppler spectrum and found better agreement with the reference sonic measurements for a medium pulse of a Doppler lidar (Manami et al., 2025).

Previous studies have demonstrated that short-range CW lidars, offering high temporal and spatial resolution and small probe volumes, have been used for turbulence measurements. Despite this, the probe volume averaging effect has not been investigated thoroughly. A key parameter for understanding this effect is the decrease in the lidar's radial velocity variance as a function of the ratio of probe volume length to turbulence scale (Mann et al., 2010). However, most field studies provide results for a limited number of probe volume lengths, typically not less than tens of metres for CW lidars, and under a narrow range of atmospheric turbulence conditions. In contrast, controlled experiments in turbulent wind tunnels allow adjustment of flow conditions and provide access to a wider range of turbulence regimes with shorter focus distances and smaller probe volumes.

The main aim of this paper is to investigate the impact of probe volume averaging on lidar-measured along-wind turbulence characteristics as a function of probe volume over integral length scale ratios. Secondly, the applicability of the Mann model (Mann, 1994) combined with a filter function, in representing the effects of probe volume averaging on turbulent spectral characteristics is evaluated across a range of probe volume to integral length scale ratios. Finally, lidar-derived turbulence statistics, including the integral length scale and radial velocity variance, are compared with hot-wire measures and the efficacy of the spectrum-based lidar variance estimation (Mann et al., 2010) is evaluated for all probe volume over integral length-scale ratios. The study is based on a dedicated experimental setup. To avoid cross-contamination of turbulent flow components and focus on probe volume averaging effects only, a staring single-beam lidar is aligned along the main flow direction in the tunnel. Hot-wire measurements are used as a reference. Open field flow characteristics are downscaled to controlled wind tunnel experiments. Tailor-made turbulent flow conditions with varying length scales and turbulence intensities are generated by an active grid in a turbulent wind tunnel. Different probe volumes of the short range CW lidar are achieved by changing the focus and position of the lidar.

This paper is organized as follows. Section 2 provides background information on the theoretical modelling of probe volume averaging and lidar velocity spectra. Section 3 describes the wind tunnel setup with detailed information about the measurement configuration, the lidar, the hot-wire anemometer and the flow properties generated by the active grid. Section 4 explains the methodology followed for the analysis of the time series velocity data and post-processing of the lidar Doppler spectrum.

https://doi.org/10.5194/egusphere-2026-825
Preprint. Discussion started: 1 June 2026


Section 5 compares the measured and Mann-based turbulent spectrum of the flow. Then, the variation in lidar-estimated integral length scales and variances is shown for all cases depending on the ratios of probe volume over integral scale. The latter section includes probability density functions of the hot-wire and the lidar velocity data for the selected cases portraying small, intermediate and large probe volume averaging for the detailed investigation of the estimated spectrum-based variances obtained from averaged Doppler spectrum of the lidar. Discussions and conclusions are given in Sections 6 and 7, respectively. Appendix A presents measured flow characteristics for all studied cases. Appendix B provides a further analysis of the factors affecting the estimation of spectrum-based variances.

This paper extends the experimental setup and measurements from (Uluocak et al., 2024) by incorporating Mann-based turbulent spectrum modelling, analysing lidar-estimated integral length scale and variance using both measurements and theoretical models. It also improves the post-processing technique for the raw lidar Doppler spectra and the calculation of integral length scale based on the autocorrelation function. Lidar radial velocity variances are estimated using both conventional approaches and the averaged Doppler spectrum method, in which the variance is obtained from the second-order moment of the averaged spectrum rather than from the fitted Gaussian width, as employed in the previous study.

## 2 Background

### 2.1 Probe volume for continuous-wave lidars

The light emitted by a lidar is not reflected from aerosols in an infinitesimally small point in space but rather from aerosols within a thin, near-cylindrical volume along the beam line-of-sight (van Dooren et al., 2022). The line-of-sight velocity $v_{\mathrm{los}}$ of the lidar can be expressed as the convolution of the weighting i.e. filtering function $\varphi(s)$ and the velocity vector $\boldsymbol{u}$,

$$v_{\mathrm{los}}(\phi,\theta,f) = \int_{-\infty}^{\infty} \varphi(s)\,\boldsymbol{n}(\phi,\theta)\cdot\boldsymbol{u}[\boldsymbol{n}(\phi,\theta)(f+s)]ds, \tag{1}$$

where $\boldsymbol{n}$ is the unity vector in the direction of the lidar beam, given by the azimuth angle $\phi$ and the elevation angle $\theta$. $f$ is the focus distance and $s$ is the distance along the line-of-sight centred at $f$. The spatial weighting function $\varphi(s)$ can be approximated as a Lorentzian weighting function for CW lidars (Sonnenschein and Horrigan, 1971):

$$\varphi(s) = \frac{1}{\pi}\frac{z_{\mathrm{R}}}{z_{\mathrm{R}}^2+s^2}, \tag{2}$$

where $z_{\mathrm{R}}$ is the Rayleigh length, i.e. the distance from the focal point at which the beam has its minimum diameter to the point where the beam's cross-sectional area is doubled compared to its minimum area (Siegman, 1986),

$$z_{\mathrm{R}} = \frac{\lambda}{\pi}\frac{f^2}{\alpha_0^2}, \tag{3}$$

https://doi.org/10.5194/egusphere-2026-825
Preprint. Discussion started: 1 June 2026


where $\lambda$ is the wavelength of the emitted laser and $\alpha_0$ is the effective radius of the aperture lens. The length of the probe volume $l_\mathrm{p}$ is considered to be equal to twice the Rayleigh length $l_\mathrm{p} = 2z_\mathrm{R}$.

### 2.2 Radial velocity spectra

We model the lidar radial velocity spectrum according to (Mann et al., 2009)

$$F_{v_\mathrm{los}}(k_1) = n_i n_j \iint |\hat{\varphi}(\mathbf{k}\cdot\mathbf{n})|^2 \Phi_{ij}(\mathbf{k}) dk_2 dk_3, \tag{4}$$

where $\hat{\varphi}$ is the Fourier transform of $\varphi$, $\mathbf{k}$ the wave vector and $\Phi_{ij}$ is the spectral velocity tensor. Equation 4 can be described as the combination of probe volume averaging along the beam direction and the one-point spectra of the velocity components, which is given as,

$$F_{ij}(k_1) = \iint \Phi_{ij}(\mathbf{k}) dk_2 dk_3. \tag{5}$$

The spectral velocity tensor $\Phi_{ij}$ is here described with the Mann model (Mann, 1994). The Mann model contains three parameters: dissipation rate $\alpha\varepsilon^{2/3}$, the length scale of turbulence $L_\mathrm{M}$, and anisotropy $\Gamma$. The parameters are usually obtained by fitting the Mann-based auto-spectra of $u_1$, $u_2$, $u_3$ ($F_{11}$, $F_{22}$, $F_{33}$), and one-point cross-spectrum of $uw$ ($F_{13}$) to, e.g., measured spectra using a two-parameter pre-computed look-up table (Peña et al., 2017).

The theoretical ratio of the radial velocity spectrum to the velocity spectrum becomes a simple relation when the radial velocity is aligned with any of the three velocity components. For a Lorentzian weighting function, this ratio is given by:

$$|\hat{\varphi}_s(k)|^2 = e^{-2|k|z_R}, \tag{6}$$

The variances and co-variances of the flow can also be obtained by integrating the spectra $F_{ij}$,

$$\sigma_{ij}^2 = \langle u_i' u_j' \rangle = \int F_{ij}(k_1)\, dk_1. \tag{7}$$

## 3 Experimental Setup

### 3.1 Measurement configuration

A measurement campaign (Uluocak et al., 2024) was conducted in the wind tunnel located at ForWind - Carl von Ossietzky Universität Oldenburg, which has $3 \times 3$ m$^2$ test section with 30 m length. The wind tunnel inflow was regulated by an active grid (Fig. 1a) installed at the tunnel inlet, designed to produce controlled and repeatable turbulent flow characteristics (Kröger et al., 2018). A single WindScanner lidar (see Sect. 3.2 for details) was used to perform measurements and a 1-D hot-wire was

https://doi.org/10.5194/egusphere-2026-825
Preprint. Discussion started: 1 June 2026


used as a reference sensor. An open test section was chosen for its ease of sensor placement and flexibility in adjusting the setup for various configurations, which were needed to have different focus distances of the lidar. Measurements were taken along the tunnel's centre line, where the influence of the open test section was considered to be the least affected region by shear layers developed along the edge of the jet flow. A minimum downstream distance of 1.5 m from the grid, equivalent to ten times the grid mesh size, was maintained. To minimize shear effects in the open test section configuration, the measurement range was limited to a maximum of 6 m downstream of the grid. Within this range, two measurement points were selected: one at 1.5 m and the other at 4.5 m downstream of the grid.

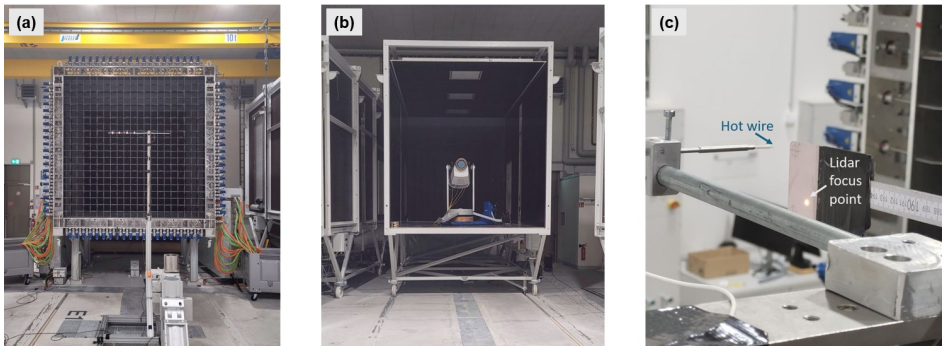


**Figure 1.** Measurement setup in the wind tunnel showing (a) the hot-wire support system downstream of the active grid, (b) the WindScanner inside the closed test section segment, (c) and the hot-wire and lidar measurement point.

The minimum probe volume size was achieved when the WindScanner was placed at 25 m downstream of the grid considering the minimum WindScanner focus distance. To generate larger probe volumes, the WindScanner was moved to the farthest possible point in the wind tunnel collector, 34 m downstream of the grid. Two WindScanner positions and two measurement points resulted in four configurations (Fig. 2) with four distinct focus lengths and corresponding probe volumes, as detailed in Table 1. To align the WindScanner beam with the incoming flow at the measurement locations, the WindScanner was levelled by positioning it within one of the wind tunnel sections. However, the transition between the wind tunnel surface and the collector platform on which the lidar was mounted had a slight ground slope, resulting in small height differences between the lidar configurations. Because the lidar was focused on the hot-wire measurement point, the resulting calibration azimuth and elevation angles differed by 2° and 1°, respectively between configurations I & II and III & IV. This difference indicates a few degrees of misalignment between the line-of-sight and the incoming flow in configurations III & IV.

To minimize flow disturbances caused by the hot-wire and its support while keeping the measurement point as close as possible, the laser beam was focused 5 cm below the hot-wire. The position of the focused laser beam was confirmed using an infrared detector card (Fig. 1c). In order to ensure a sufficient number of aerosols in the wind tunnel for optimal back scattering, a seeding generator was used during the measurements. The wind tunnel was run for one minute to ensure the flow reached a statistically stationary state prior to activating the active grid.

https://doi.org/10.5194/egusphere-2026-825
Preprint. Discussion started: 1 June 2026


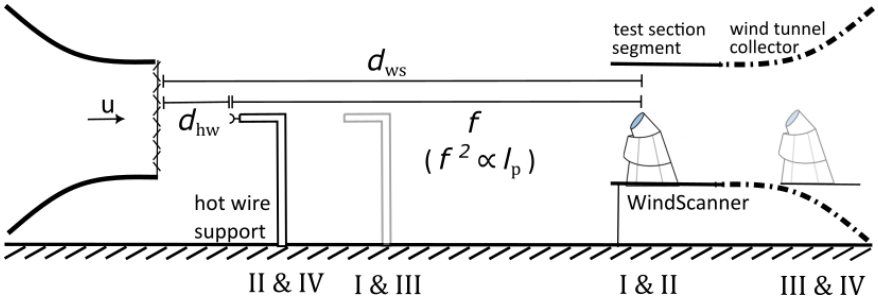


**Figure 2.** Measurement configurations showing the generation of four different focus lengths ($f$) by changing the downstream position of the hot-wire ($d_{\mathrm{hw}}$) and the WindScanner ($d_{\mathrm{ws}}$). The corresponding values for each case are given in Table 1.

**Table 1.** Downstream positions of the hot-wire ($d_{\mathrm{hw}}$) and WindScanner ($d_{\mathrm{ws}}$) from the active grid with the corresponding focus lengths ($f$) and probe volumes ($l_{\mathrm{p}}$).

| configuration | $d_{\mathrm{hw}}$ [m] | $d_{\mathrm{ws}}$ [m] | $f$ [m] | $l_{\mathrm{p}}$ [m] |
|---|---|---|---|---|
| I | 4.5 | 25 | 20.5 | 0.14 |
| II | 1.5 | 25 | 23.5 | 0.19 |
| III | 4.5 | 34 | 29.5 | 0.28 |
| IV | 1.5 | 34 | 32.5 | 0.34 |

### 3.2 Wind speed measurement devices

The WindScanner is a continuous-wave short-range scanning wind lidar designed by the Technical University of Denmark, DTU (Mikkelsen, 2014). As is the case for all Doppler lidars, it determines the velocity of aerosol particles in the atmosphere by measuring the Doppler shift, i.e., the frequency change ($\delta\nu$) of the backscattered signal from aerosols. The wavelength of the emitted light is 1.55 $\mu$m and the effective radius of the aperture lens is 56 mm. WindScanner can measure line-of-sight velocity within the range [-30,30] m s $^{-1}$. It can be operated between the focus distances of 20 m to 300 m with a maximum sampling frequency of 451.7 Hz. The WindScanner's rotating head with two prisms allows users to do quick and pre-defined scans. Scans can be synchronised with dual or triple WindScanner configurations. However, for this study, only single WindScanner staring measurements were performed by aligning the line-of-sight with the main wind direction.

Measurements were performed with four focus distances varying between 20.5 and 32.5 m and probe volumes of 0.14 m to 0.34 m with the maximum sampling frequency of 451.7 Hz. The backscattered light was sampled at a frequency of 120 MHz, and the resulting Doppler spectra were computed using 512 frequency bins, which yields a wind speed resolution of $0.2310^{-6}$ Hz corresponding 0.183 m s$^{-1}$. The uncertainty of the WindScanner measured radial velocity has been demonstrated to be approximately 0.1 % based on the results of a wind tunnel calibration study (Pedersen and Courtney, 2021).

https://doi.org/10.5194/egusphere-2026-825
Preprint. Discussion started: 1 June 2026


A single lidar can provide only the line-of-sight radial velocity, which represents the projection of the three-dimensional flow velocity components along the lidar beam direction. However, since we align the lidar beam with the mean wind direction, the along-velocity component $u$ is assumed to be equal to the line-of-sight velocity.

Reference wind speed measurements were performed using 1-D Dantec Dynamics hot-wire probe type 55P16 with 20 kHz sampling frequency. The sensor was mounted at the centre of open test section on a structure with an extended rod and aligned with the mean flow direction. It was calibrated every day during the measurement campaign using a StreamLine Pro Automatic Calibrator, whilst taking into account a temperature correction. The temperature was recorded as approximately $20\,^{\circ}$C in the tunnel during the campaign in August 2024. The calibration curve had less than 1 % relative error for the velocity range of 0.5 m $s^{-1}$ to 20 m $s^{-1}$. Synchronization between the hot-wire and WindScanner data was achieved using a trigger signal generated by the active grid protocol, ten seconds after its initiation.

### 3.3 Active grid generated flows

The active grid, developed by ForWind at Carl von Ossietzky Universität Oldenburg, is capable of generating customized Gaussian and non-Gaussian turbulence and gust structures (Schottler et al., 2017), achieving high Taylor Reynolds numbers (Neuhaus et al., 2021), and mimicking and reproducing measured atmospheric flows (Kröger et al., 2018). Various turbulent flow patterns are produced through the independent control of multiple shafts, each fitted with rectangular flaps. The characteristics of the turbulence generated by the active grid are primarily governed by two parameters: the flap angle $\alpha$ and the rate of change of this angle over time $\delta\alpha/\delta t$. The flap angle $\alpha$ adjusts the local blockage at the inlet, ranging from 20 % to 92 %, which is primarily utilized to modulate wind shear and turbulence intensity profiles and defined as static -flap- protocols. Meanwhile, the time derivative $\delta\alpha/\delta t$ influences the turbulent spectra and the associated length scales (Neuhaus et al., 2021) in dynamic -flap- protocols. The relationship between the active grid settings and the resulting flow dynamics is described by a transfer function (Kröger et al., 2018), which serves as an input for the grid control program to achieve the desired inflow conditions (Neuhaus et al., 2021).

After performing the tests with the desired inflow conditions, the actual flow parameters were recalculated from the recorded hot-wire measurements. The presented integral length scale was estimated by computing the auto-correlation function of the hot-wire signal and integrating up to the $1/e$. For each of the four measurement configurations (Table 1), eight active grid protocols (Table 2) were used to generate various turbulent flow conditions with a mean wind speed of approximately 7.5 m $s^{-1}$.

To investigate the effect of the probe volume averaging, integral length scales both smaller and larger than the probe volumes were produced to obtain the representative probe volume over length scale ratios as in the atmosphere. The minimum integral length scale generated was 0.03 m, with a turbulence intensity (TI) of 7 %, achieved by maintaining a fixed flap angle of $80^{\circ}$ (protocol 4). The largest estimated length scale was 1.7 m, with a TI of 12 %, generated by dynamically varying the flap angle around a mean angle of $\alpha = 60^{\circ}$ with a $15^{\circ}$ variation over time (protocol 7). The generated integral length scale $L$ and the turbulence intensity of the flow for all protocols and configurations are presented in Fig. 3 and all values are given in Table A1 in Appendix. Same figure shows a consistent mean velocity increase from configurations II & IV (at 1.5 m downstream) to

https://doi.org/10.5194/egusphere-2026-825
Preprint. Discussion started: 1 June 2026


**Table 2.** Active grid protocols used to generate different flows by changing grid flap angle ($\alpha$) and the flap angle over time $\delta\alpha/\delta t$

| protocol | grid status | $\alpha$ [°] | $\delta\alpha/\delta t$ [] |
|---|---|---|---|
| 1 | static | 20 | - |
| 2 | static | 40 | - |
| 3 | static | 60 | - |
| 4 | static | 80 | - |
| 5 | dynamic | 20 | 7.5 |
| 6 | dynamic | 40 | 10 |
| 7 | dynamic | 60 | 15 |
| 8 | dynamic | 40 | 12.5 |

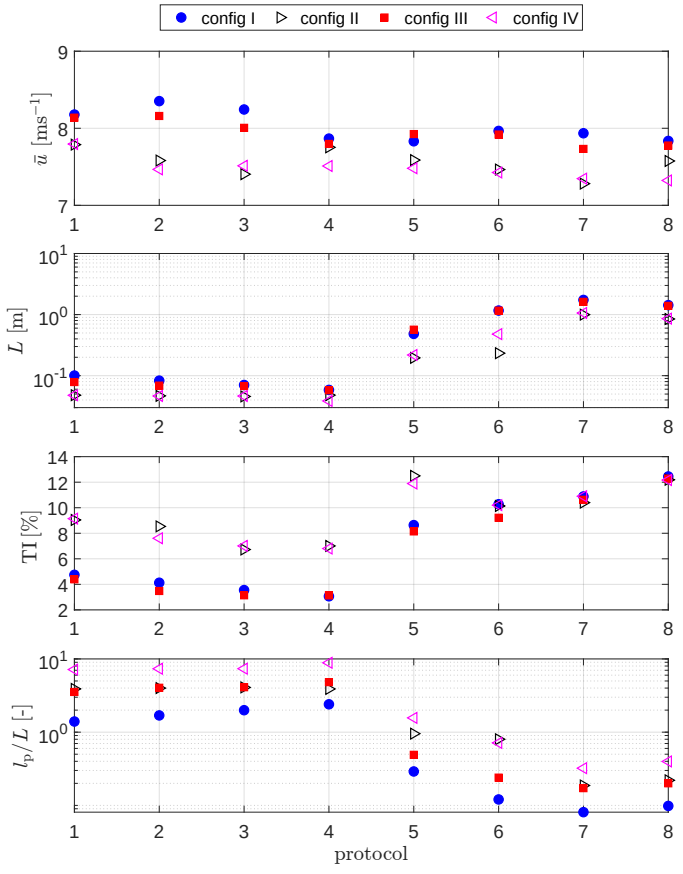


**Figure 3.** Hot-wire measured mean wind velocity $\bar{u}$, integral length scales $L$ and the turbulence intensity TI of the flows generated by the active grid protocols for four configurations defined in Table 1. The bottom plot shows the probe volume of the lidar over integral length scale ratios for all measurement cases.

https://doi.org/10.5194/egusphere-2026-825
Preprint. Discussion started: 1 June 2026


configurations I & III (at 4.5 m downstream), as evidenced by hot-wire. Variations in flow properties between configurations arise due to differences in flow development at different downstream positions.

With the generated length scales and corresponding probe volumes belonging to that configuration, ratios of probe volume over length scale $l_\mathrm{p}/L$ were estimated, ranging from 0.08 to 8.85 (in Fig. 3). To assess whether these ratios are representative of typical lidar ABL measurement conditions, integral length scales and lidar probe volume lengths reported in the literature are summarized. Integral length scales in the atmospheric boundary layer vary with stability regime. Under convective conditions, integral scales scale with the boundary layer depth and can reach several hundred metres to over a kilometre (Zhou et al., 2020). In neutral conditions, typical values increase with height and range from approximately 10 m to 350 m (Nandi and Yeo, 2021). Stable boundary layers are shallower and characterized by weaker turbulence, resulting in smaller integral scales, typically between 1 m and 100 m (McWilliams et al., 2023). Based on atmospheric open field measurements reported in the literature, the probe volume lengths of commonly used lidar systems range from approximately 7 m to 28 m for CW WindScanners (focus distances of 145 m to 296 m) (Sekar et al., 2024), 7 m to 26 m for the SpinnerLidar (focus distances of 53 m and 103 m) (Mikkelsen et al., 2013), probe volumes are reported as 29 m for the WindEye system at an 93 m focus length (Dellwik et al., 2015), 30 m for the ZX 300 lidar at 200 m focus distance (Knoop et al., 2021) and 50 m for long-range pulsed Windcube 200S (Puccioni and Iungo, 2021). The resulting ratios, derived from ABL lidar measurements, are shown in Fig. 4 together with the corresponding ratios obtained from wind tunnel measurements. It shows that the generated prove volume over length scale ratios fit quite well the most relevant range in the open field.

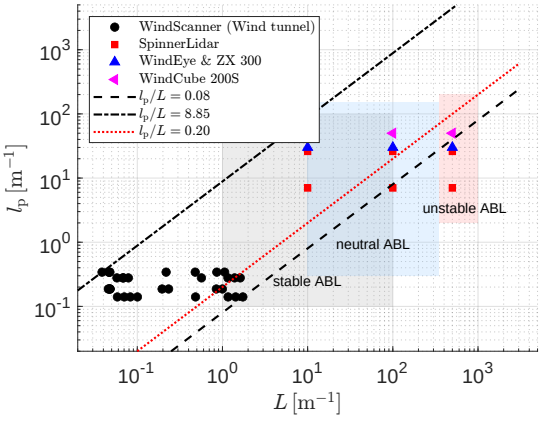


**Figure 4.** Probe volume lengths ($l_p$) of common lidar systems across ABL regime length scales ($L$) with corresponding probe volume over length scale ratios.

Figure 5 shows the turbulence spectrum of the hot-wire velocity measurements for the number of generated flows. The lower energy level at high frequencies in configuration I & III compared to configuration II & IV agrees with the lower measured TI values in Fig. 3 caused by the different hot-wire positions i.e. flow characteristics. As observed, cases generated by static grid protocols have a similar spectrum to that of conventional atmospheric flow i.e. atmospheric-like, with a relatively flat shape at

https://doi.org/10.5194/egusphere-2026-825
Preprint. Discussion started: 1 June 2026


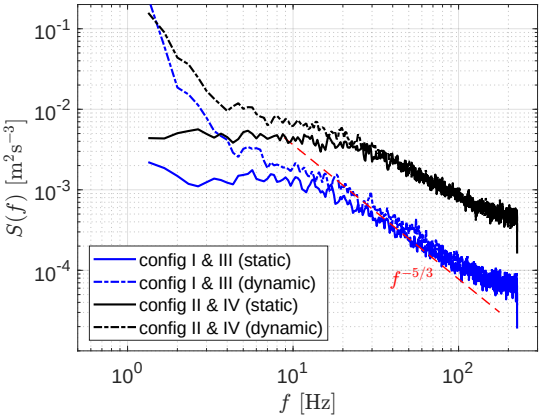


**Figure 5.** Velocity spectra of the hot-wire measurements for different configurations and grid protocols. Identical hot-wire positions in configurations I & III and II & IV result in the repetition of the same flow cases, which are therefore shown as a single spectrum. The Kolmogorov -5/3 slope in the inertial range is indicated by the dashed line.

low frequencies followed by a -5/3 inertial subrange, while the cases with dynamic protocol show much higher energy at low frequencies.

The Mann turbulence model assumes homogeneous, stationary atmospheric turbulence with shear-induced anisotropy and locally isotropic small scales (Mann, 1994). Consequently, the model is applicable when the measured velocity spectra exhibit a conventional atmospheric spectra shape as observed in the static protocol's spectra in Fig. 5. Deviations from this behaviour at very low frequencies are observed in the dynamic protocol's spectra, often associated with non-stationarity and large-scale phenomena, are not described by the Mann model and were therefore excluded from the modelling. Consequently, the Mann model was only implemented on the static cases, resulting in 16 out of 32 cases with protocol numbers 1 to 4.

## 4 Methodology

### 4.1 Data acquisition

The mean tunnel wind speed was initially set to 7.5 m s$^{-1}$ and left running for one minute before each measurement. In each case, ten minutes of data were recorded; however, a six-minute period was used for statistical analysis to ensure consistency across all cases, as in some instances the lidar recorded data for only six minutes. The hot-wire data recorded with 20 kHz were downsampled to match the WindScanner sampling frequency of 451.7 Hz using linear interpolation. The resolution of the lidar velocity was 0.18 m s$^{-1}$, while the hot-wire resolution was found to be less than 0.05 m s$^{-1}$. For comparative analysis of hot-wire and lidar variances, the effect of different resolution of measurement systems were eliminated by rounding the hot-wire velocity values with the lidar resolution. The maximum change in the hot-wire variance was found to be 0.02 m$^2$ s$^{-2}$ for the highest turbulence flow cases.

https://doi.org/10.5194/egusphere-2026-825
Preprint. Discussion started: 1 June 2026


### 4.2 Post-processing of lidar Doppler radial velocity spectrum

While commercial lidars provide estimates of radial velocity, in this study it is calculated directly from the dominant frequency of the raw Doppler signals using three methods (maximum, centroid, and median). Since these methods only use the dominant frequency information to determine $v_{\mathrm{los}}$, the computed turbulence statistics from those velocities are filtered and therefore sometimes referred to as 'filtered' turbulence statistics (Fu et al., 2023). Additionally, the Doppler spectra are averaged and the second order moment of the averaged spectrum is used to obtain spectrum-based lidar radial velocity variance i.e. so-called 'unfiltered' velocity variance. Prior to estimating the radial velocity from the dominant frequency or averaging Doppler spectra, it is necessary to remove noise spectrum from each lidar Doppler spectrum. The noise spectrum consists of a background measurement noise and sometimes can appear appear as secondary peaks caused by backscatter from hard targets. Removing the noise spectrum is particularly important for the spectrum-based turbulence statistics, since the shape of the averaged spectrum significantly affects its second-order moment i.e. radial velocity variance. In this study, four cases containing hard target noise spectrum originating from the moving grid flaps (Figure B1), were identified and removed from the dataset (Appendix B1).

The Doppler radial velocity spectrum of this CW lidar exhibits a main peak corresponding to the dominant velocity, a negative peak at zero velocity, and a bumpy background noise, with a bump centred around zero radial velocity as shown in Fig. 6a. Sometimes, only a pronounced peak appears around zero radial velocity due to lidar noise, which should be removed as well.

For all the individual raw lidar spectra, we first removed the non-flat background noise: for each 6-min segment, the noise was determined by computing the median of the half of the Doppler radial velocity spectrum, where the main peak was not present and then we mirrored it to the other half (Fig. 6a). Each Doppler radial velocity spectrum was then normalized by this computed background noise, which resulted in a flat background noise around unity (Fig. 6b). Finally, the flat background noise was removed using a threshold set to 'three' standard deviations above the mean noise spectrum level, which was determined by using the spectrum values within the first 20 bins, following the approach described by Angelou et al. (2012) (Fig. 6c). Each Doppler radial velocity spectrum background level was then shifted from one to zero and normalized with its area (Fig.6d). The radial velocity can then be estimated from the dominant frequency of the clean Doppler radial velocity spectrum at this step using one of these conventional methods (maximum, centroid, and median).

The carrier-to-noise ratio (CNR) is estimated by calculating the ratio of clean Doppler radial velocity spectrum area to background noise area (van Dooren et al., 2022). It was found to be approximately -18 dB for all cases, resulting in almost no filtering of radial velocities when using a -22 dB threshold. An outlier removal procedure was applied to the lidar radial velocities using a threshold of three standard deviations of radial velocities, which resulted in less of 1% of data loss for each case. Figure 7 shows 30 sec time series of along-wind velocities of the lidar obtained from centroid method and the hot-wire for three cases portraying the smallest, intermediate and the largest probe volume averaging. The agreement between the hot-wire and lidar mean velocities for all methods exhibits an RMSE of 0.18 m $s^{-1}$ or less across all cases, which is considered sufficient for analysing turbulence statistics between the two measurement systems.

https://doi.org/10.5194/egusphere-2026-825
Preprint. Discussion started: 1 June 2026


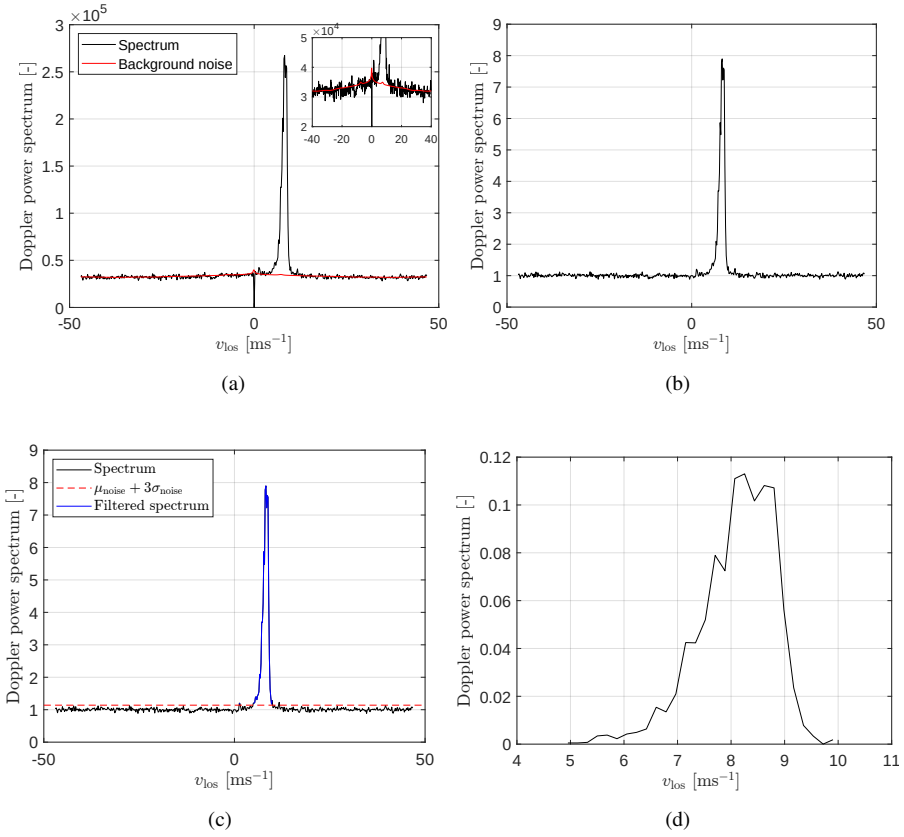


**Figure 6.** Sequence of processing raw lidar Doppler spectra (a) Original individual radial velocity spectrum (black) and the estimated non-flat background noise (red). (b) Radial velocity spectrum after normalization by the background noise level. (c) Threshold applied to the normalized spectrum and the resulting cleaned spectrum (blue). (d) Cleaned and area-normalized spectrum.

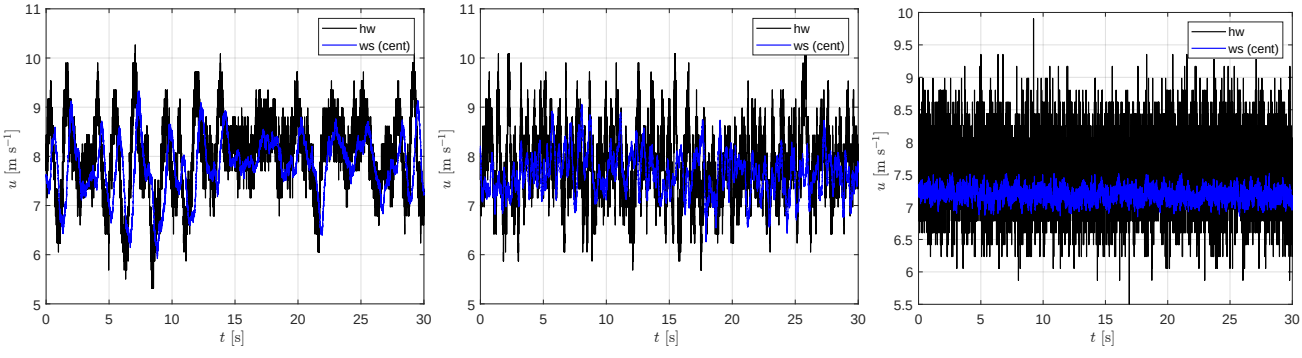


(a) $l_p/L = 0.08$ (config. I & protocol 7) (b) $l_p/L = 0.30$ (config. I & protocol 5) (c) $l_p/L = 8.85$ (config. IV & protocol 4)

**Figure 7.** 30 s time series of along-wind velocity measured by the hot-wire (hw) and the WindScanner (ws) for three cases with the smallest (a), intermediate (b), and largest (c) $l_p/L$ ratios.

https://doi.org/10.5194/egusphere-2026-825
Preprint. Discussion started: 1 June 2026


For the spectrum-based turbulence statistics, all clean Doppler spectra were ensemble-averaged and interpreted as a probability density function (PDF) given by $p(v_\mathrm{r})$ of the lidar radial velocities $v_\mathrm{r}$, where the mean $\mu_{v_\mathrm{r}}$ and the variance $\sigma^2_{v_\mathrm{r}}$ are derived from the first and the second order moment of the area-normalized PDF, respectively as,

$$\mu_{v_\mathrm{r}} = \int_{-\infty}^{\infty} v_\mathrm{r} p(v_\mathrm{r})\,\mathrm{d}v_\mathrm{r} \tag{8}$$

$$\sigma^2_{v_\mathrm{r}} = \int_{-\infty}^{\infty} (v_\mathrm{r} - \mu_{v_\mathrm{r}})^2 p(v_\mathrm{r})\,\mathrm{d}v_\mathrm{r} \tag{9}$$

## 5 Results

The results are divided into two main parts. In Sec. 5.1, we use 16 atmospheric-like measurement cases and compare measured and Mann-modelled turbulent spectra of the flow, and investigate probe volume averaging based on the turbulent velocity spectra. In Sec. 5.2 we compare the lidar-derived integral length scale and velocity variance to the hot-wire measures depending on probe volume over integral length scale ratios. In the same section, the spectrum-based velocity variance so-called 'unfiltered' variance is estimated from the PDF of averaged lidar Doppler spectrum across all cases. In addition, we present PDFs of the selected cases portraying the smallest, intermediate and the largest probe volume averaging.

### 5.1 Measured and Mann-based turbulent spectrum of the flow

We can extract turbulence characteristics of the wind tunnel flow cases by fitting the Mann model to the hot-wire velocity measurements. The fitting procedure is described in Peña et al. (2017). Deviating from this procedure, here we estimate the Mann parameters by minimizing the error on the $u$-velocity spectrum using Mann-based pre-computed look-up-tables instead of the three velocity spectra and $uw$-co-spectrum as traditionally done for atmospheric flows (Peña, 2019). Once the Mann parameters are known, we can derive both the Mann-based $u$-velocity spectrum (Eqn. 5) and the Mann-based lidar radial velocity spectrum (Eqn. 4), which is impacted by the filtering function (Eqn. 6). The Mann model was adjusted to the 16 selected subset of the wind tunnel cases when the hot-wire spectrum exhibited close to atmospheric turbulence characteristics, e.g., the presence of a single peak in the pre-multiplied velocity spectrum (see Section 3.3). The estimated Mann model parameters are presented in Fig. 8. Mann-based turbulence length scales $L_M$ are found to be on the order of centimetres, which aligns with the estimated length scales of hot-wire data for these cases. Notably, half of the the fitted dissipation rate $\alpha\epsilon^{2/3}$ values at high TI are significantly higher than those under typical atmospheric conditions, which range from zero to 0.5 $\mathrm{m}^{4/3}\mathrm{s}^{-2}$.

Furthermore, Figure 8 shows that flows generated using the same active grid protocols are described by similar Mann parameters, demonstrating the repeatability of wind tunnel flows within the Mann model framework except one case. One flow case has a significantly different Mann-based turbulence length scale and dissipation rate in comparison to its repeated

https://doi.org/10.5194/egusphere-2026-825
Preprint. Discussion started: 1 June 2026


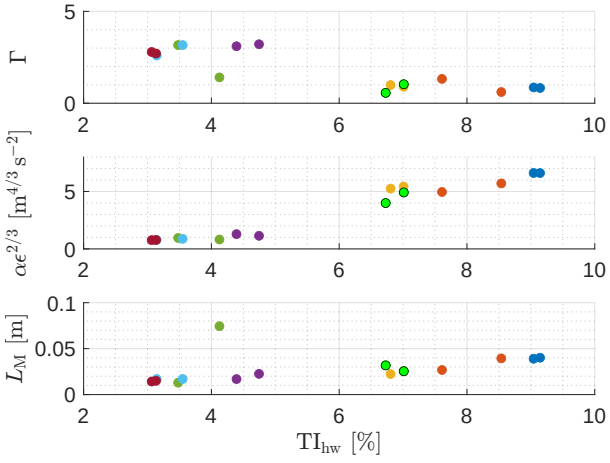


**Figure 8.** Mann parameters as function of hot-wire TI for 16 wind tunnel cases. Flows are generated using 8 active grid protocols while keeping the hot-wire position fixed, resulting in the repetition of the same 8 cases. The colour-paired dots represent flows generated by repeated protocols. The green dot with black outline represents protocol 3, configurations II & IV which were used for further analysis.

flow case, due to differences in the peak spectrum at high frequency region resulting in a different Mann model fit to that spectrum. A high correlation was identified between the variance predicted by the Mann model (Eqn. 7) and that measured by the hot-wire, with a coefficient of determination $R^2 = 0.99$ and no bias.

Figure 9 compares the hot-wire and WindScanner velocity spectra for two cases with similar flow conditions (configurations II and IV using protocol 3) but different lidar probe volume sizes of 0.19 m$^{-1}$ and 0.34 m$^{-1}$, respectively. The Mann-modelled hot-wire and lidar velocity spectra are also shown in the figure. The filtering of the lidar spectrum compared to the hot-wire spectrum can be seen by reduced energy across all wave numbers $k$. The impact of probe volume averaging is also clear from the reduced energy with the increasing probe volume. The energy increase at high frequencies (i.e., wave numbers beyond 10 m$^{-1}$) in the lidar data is attributed to lidar measurement noise, as reported in several studies (Angelou et al., 2012; Peña et al., 2017; Peña and Mann, 2019; van Dooren et al., 2022). The Mann model accurately fits the measured hot-wire spectra up to the cut-off wave number $k_{\mathrm{cutoff,hw}}$= 70 m$^{-1}$, after which the measurement noise dominates. A minor discrepancy is observed between the Mann models of the repeated hot-wire measurements, with one spectrum exhibiting slightly higher energy levels than the other, particularly for wave numbers below 10 m$^{-1}$.

The Mann-modelled lidar spectra show good agreement with the measured lidar spectra for the configuration II with $l_{\mathrm{p}} = 0.19\,\mathrm{m}$ resulting in a matching spectra for wave numbers up to $k_{\mathrm{cutoff,ws}}$ =7 m$^{-1}$ where the lidar energy level is at its peak. In contrast, for configuration IV with $l_{\mathrm{p}} = 0.34\,\mathrm{m}$, the Mann-modelled lidar spectra systematically overestimate the measured lidar spectra. This overestimation coincides with higher energy levels of the Mann-modelled hot-wire spectra used as input for the lidar spectra modelling. The measured lidar energy level peak of 2.7 m$^{-1}$ is shown as the cut-off wave number for this case.

We estimate the spectral ratio of the lidar radial velocity to that of the $u$-velocity of the hot-wire across all wave numbers to evaluate probe volume averaging effects. Figure 10 presents the ratio of the WindScanner radial velocity spectra to the hot-wire

https://doi.org/10.5194/egusphere-2026-825
Preprint. Discussion started: 1 June 2026


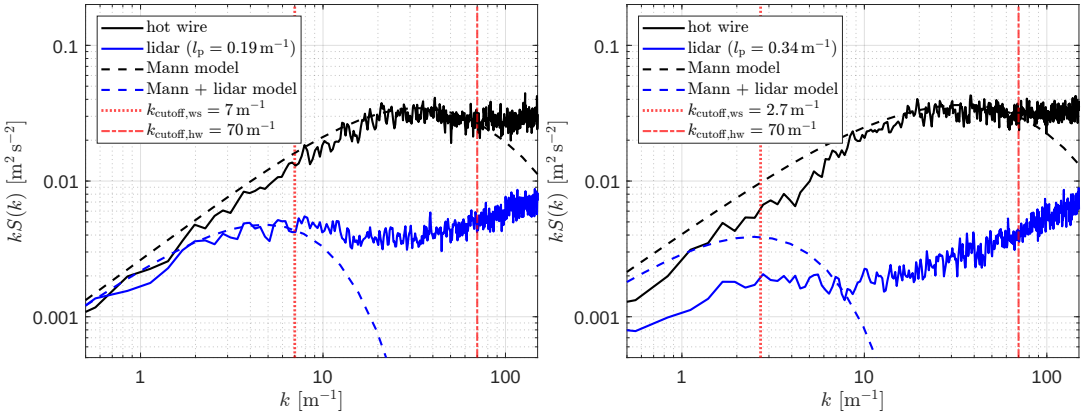


(a) Config. II & protocol 3 ($l_p = 0.19$ m) (b) Config. IV & protocol 3 ($l_p = 0.34$ m)

**Figure 9.** Along-wind velocity spectra from the hot-wire and lidar, alongside Mann model spectra, for two different lidar configurations (i.e., lidar probe volumes).

velocity spectra, along with the modelled spectral ratio for 8 atmospheric-like cases having the smallest and the largest probe volume $l_\mathrm{p}$. For each case, the measured spectra ratio decreases with increasing wave number due to probe volume averaging, while a rise at higher frequencies (>10 m$^{-1}$) is attributed to lidar/hot-wire measurement noise. As $l_\mathrm{p}$ increases, the measured spectral ratio decreases. This trend is also reflected in the modelled ratios when $l_\mathrm{p}$ changes from 0.14 m to 034 m.

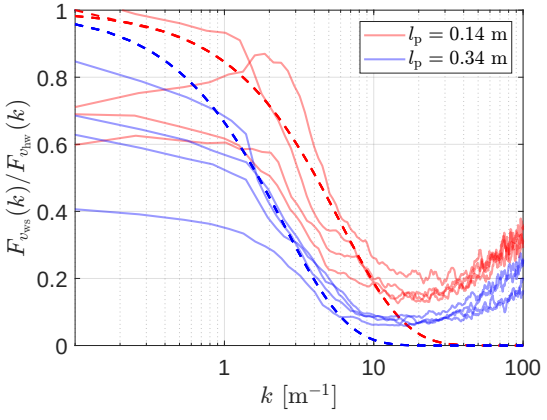


**Figure 10.** Measured (solid) and modelled (dashed) velocity spectra ratio of the WindScanner's radial velocity to the hot-wire velocity, for 8 atmospheric-like spectra cases in which static grid protocols were used, having the smallest and the largest probe volumes $l_\mathrm{p}$. Modelled ratios are estimated from Eqn. 6.

https://doi.org/10.5194/egusphere-2026-825
Preprint. Discussion started: 1 June 2026


### 5.2 Measurement of integral length scale and variance

The integral length scale is determined by integrating the auto-correlation function up to $1/e$ for the hot-wire, lidar and filtered hot-wire data. Hot-wire velocities are filtered using the Lorentzian weighting function to simulate lidar probe volume averaging. Figure 11 presents the ratio of the lidar and filtered hot-wire integral length scales to the reference hot-wire length scale for all cases as a function of $l_\mathrm{p}/L$. This figure highlights the challenges of estimating turbulence parameters from lidar measurements, also referred to as the lidar-turbulence paradox (Peña et al., 2025); here in particular, estimation of the turbulent length scale from lidar measurements requires prior knowledge of the turbulence conditions. The general trend of the integral length scale ratio is consistent with both the lidar and filtered hot-wire data, despite some discrepancies. These discrepancies may arise from differences in measurement noise between the lidar and hot-wire data, as well as the downsampling of the hot-wire data prior to the application of lidar filtering. For small $l_\mathrm{p}/L$ (< 0.2) values, lidar estimates of the integral length scales agree well with the one obtained from reference hot-wire data. As $l_\mathrm{p}/L$ increases, the lidar and filtered hot-wire data progressively overestimate the integral length scale since small scale turbulence is attenuated by probe volume averaging. The overestimation of lidar-derived length scales ranges between 6 % and 100 % with the increasing probe volume over length scale ratios used in this study.

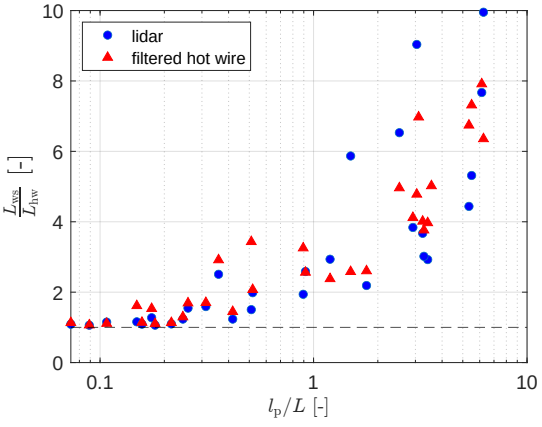


**Figure 11.** The ratio of the integral length scales derived from lidar and filtered hot-wire data to the reference integral length scale of the hot-wire for all cases, as a function of $l_\mathrm{p}/L$. The dashed line indicates the ideal value of 1.

Figure 12 shows the ratio of the velocity variance of WindScanner to hot-wire measurements depending on $l_\mathrm{p}/L$. The WindScanner velocity variance is estimated from the statistics of $v_\mathrm{los}$ which was obtained using three methods (centroid, maximum, median) and from the second order moment of the averaged lidar Doppler spectrum. The ratio of the theoretical velocity variance of the WindScanner and the hot-wire was estimated from the integration of Mann-modelled lidar spectra to the hot-wire spectra. The line with the velocity variance ratio equal to 1 is plotted to show the ideal case where the lidar can capture the velocity fluctuations as the hot-wire. The ratio values smaller than 1 correspond to an underestimation of variance by the lidar and values larger than 1 state an overestimation compared to the hot-wire variance values. It is evident that there is

https://doi.org/10.5194/egusphere-2026-825
Preprint. Discussion started: 1 June 2026


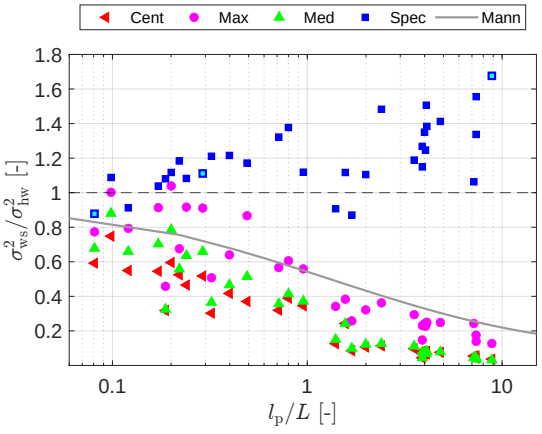


**Figure 12.** Ratio of the velocity variance from WindScanner to hot-wire measurements for varying $l_{\mathrm{p}}/L$ values. The WindScanner velocity variance is estimated from the statistics of $v_{\mathrm{los}}$ using three methods (centroid, maximum, median) and from the second order moment of averaged Doppler spectrum of the lidar (Spec) where three highlighted points are the selected cases to show the differences between the smallest, intermediate and the largest probe volume averaging. The solid line indicates the theoretical ratio of the Mann-based lidar variance to the hot-wire variance. The dashed line indicates the ideal value of 1.

an underestimation of the velocity variances of the lidar obtained from $v_{\mathrm{los}}$ statistics using the maximum, median, and centroid method due to the probe volume averaging.

The variance ratio differs between methods, with the maximum method showing the least underestimation. The modelled variance ratio is consistent with the measured variance ratio of the maximum method, showing an underestimation of velocity variance reaching up to 80 % where the maximum probe volume averaging occurs at $l_{\mathrm{p}}/L$ = 8.85. However, the velocity variance obtained from the averaged Doppler radial velocity spectrum of the lidar does not show underestimation as $l_{\mathrm{p}}/L$ increases, which indicates compensation for the effect of probe volume averaging. Yet, the variance remains overestimated in most cases, with the degree of overestimation varying across cases. The spectrum-based variance ratio varies between 0.8 and 1.7, with an average value of 1.20.

To understand the differences between the hot-wire and spectrum-based lidar variances, the PDFs of the hot-wire velocity measurements and the averaged Doppler radial velocity spectrum of the lidar are plotted for the cases with smallest, intermediate and largest probe volume averaging in Fig. 13. In the case of the smallest $l_{\mathrm{p}}/L$, i.e. minimum probe volume averaging (Fig. 13a), the PDF of the hot-wire and the averaged lidar spectrum data are both slightly left-skewed. Although the averaged lidar spectrum PDF can capture this behaviour to the greatest extent, even slight differences at the tails of the PDF resulted in 0.1 $\mathrm{m^2 s^{-2}}$ underestimation of variance. For the intermediate probe volume averaging case (Fig. 13b), the PDFs are more symmetrically distributed for both hot-wire and the lidar but the lidar PDF is wider, which results in a small overestimation of the variance. In the case of the largest $l_{\mathrm{p}}/L$ (Fig. 13c), the lidar PDF exhibits additional velocity contributions around bins close to 5.5 m $\mathrm{s^{-1}}$, which results in significant overestimation of the variance compared to that of the hot-wire.

https://doi.org/10.5194/egusphere-2026-825
Preprint. Discussion started: 1 June 2026


To assess whether the asymmetric or additional velocity bins originate from a few dominant peaks or from consistent be-
375 haviour across all spectra, the individual lidar Doppler radial velocity spectra are plotted in Fig. 14. It is clearly seen that the asymmetric or wider PDFs do not result from few number of high-amplitude noise peaks, but rather from the overall distribution of the individual spectra in Figures 14a and 14b. Figure 14c shows that all individual spectra passes around 5.5 m s$^{-1}$, which is also present in the corresponding averaged spectrum PDF.

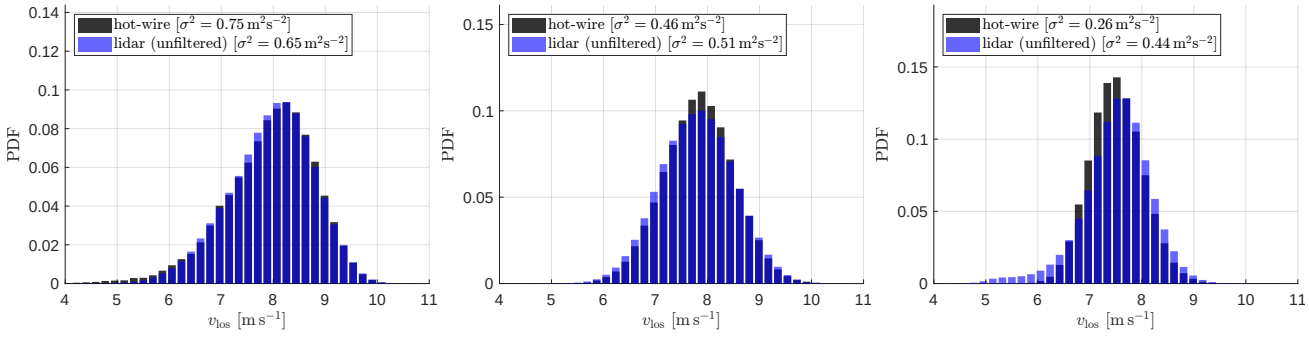


(a) (a) $l_p/L = 0.08$ (config. I & protocol 7) (b) (b) $l_p/L = 0.30$ (config. I & protocol 5) (c) (c) $l_p/L = 8.85$ (config. IV & protocol 4)

**Figure 13.** PDF of the hot-wire velocity time series and the averaged Doppler spectrum of the lidar (so-called 'unfiltered') for three cases corresponding to one of the smallest (a), intermediate (b), and largest (c) $l_p/L$ ratios. The bin width is the same as the lidar resolution of 0.18 m s$^{-1}$. The hot-wire and lidar PDFs are aligned by their mean values to facilitate comparison of PDF width.

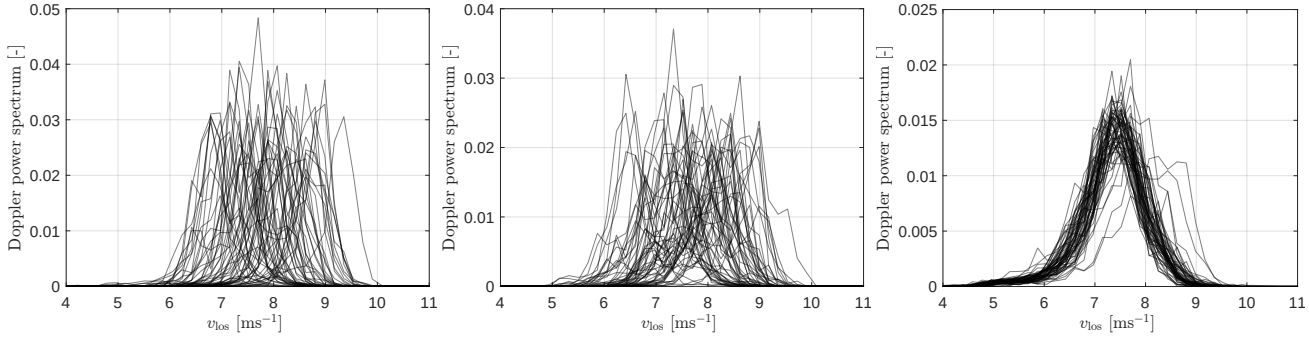


(a) (a) $l_p/L = 0.08$ (config. I & protocol 7) (b) (b) $l_p/L = 0.30$ (config. I & protocol 5) (c) (c) $l_p/L = 8.85$ (config. IV & protocol 4)

**Figure 14.** One-minute lidar spectra for three cases corresponding to one of the smallest (a), intermediate (b), and largest (c) $l_p/L$ ratios. To aid visualization, the spectra are derived from 1 s time series, resulting in 60 spectra displayed over the one-minute interval.

The factors influencing the estimation of velocity variance due to post-processing of the individual Doppler radial velocity
380 spectra are further examined in Appendix B. The selection of noise removal threshold affects the spectrum-based variance (Figure 6c). Increasing the noise threshold reduces the wider portion of the spectrum and leading to a lower estimated variance. Analysis show that averaged estimated variance ratios decreased from 1.37 to 1.13 as the threshold increased from 1 $\sigma_{\mathrm{noise}}$ to

https://doi.org/10.5194/egusphere-2026-825
Preprint. Discussion started: 1 June 2026


$5\,\sigma_{\mathrm{noise}}$ (Appendix B2). Similarly, the effect of the normalization methods on variance estimation is analysed in Appendix B3. It was found that using peak normalization instead of area normalization results in an average increase in the variance ratio of 0.08.

Velocity gradients along the probe volume lead to an increase in the spectrum-based estimate of velocity variance. The influence of such gradients is quantified following the reference approach of (Mann et al., 2010), in which the additional broadening of the PDF caused by a velocity gradient is corrected using a modified distribution obtained from the convolution of a Gaussian and a Lorentzian function, provided that the gradient along the probe volume is known. To quantify the velocity gradient along the probe volume, we first calculated the velocity gradient along the wind tunnel. Mean hot-wire velocity measurements show that from configurations II & IV (at 1.5 m) to configurations I & III (at 4.5 m), the velocity increases between $0.2\,\mathrm{m\,s^{-1}}$ to $0.7\,\mathrm{m\,s^{-1}}$ under identical grid protocols i.e. flow conditions (Figure 3). Assuming a linear velocity gradient over the 3 m tunnel length, the corresponding velocity differences across the probe volumes (0.14 m, 0.19 m, 0.28 m, and 0.34 m) are estimated to range between $0.01\,\mathrm{m\,s^{-1}}$ and $0.07\,\mathrm{m\,s^{-1}}$ for all cases. After applying the PDF width correction based on this gradient, the average variance ratio decreases by up to 0.10, resulting in an average unfiltered variance ratio of 1.10 (Figure B3).

The analysis shows that both the noise-removal threshold and the velocity gradient have a significant influence on the spectrum-based variance estimation. Although increasing the noise threshold reduces the estimated variance, a conservative $3\,\sigma_{\mathrm{noise}}$ threshold is already applied in the present analysis; therefore, the choice of noise threshold alone cannot explain the observed variance overestimation. In contrast, the results indicate that velocity gradients within the probe volume play a dominant role in the systematic overestimation observed across most cases.

## 6 Discussion

The dedicated measurement setup of a turbulent wind tunnel and a CW lidar facilitated 32 distinct probe volume over integral length scale ratios ranging from 0.08 to 8.85. This enabled the systematic investigation of the effects on the sensing of along-wind turbulence characteristics.

The Mann model was fitted to the hot-wire spectra, and the corresponding Mann-based lidar spectra were obtained by combining the hot-wire model spectra with the lidar filtering function. Overall, the Mann model shows good agreement with the measured hot-wire spectra (Fig. 9a and 9b). The minor discrepancies observed between the modelled hot-wire spectra for repeated hot wire flow cases may be attributed to small variations in experimental configuration, flow conditions, or uncertainties associated with the fitting methodology. Although good agreement is generally observed between the hot-wire measurements and the Mann model parameters, the dissipation rate parameter $\alpha\epsilon^{2/3}$ is found to be higher than values typically reported for atmospheric turbulence. These elevated $\alpha\epsilon^{2/3}$ values can be attributed to the compensation required to accommodate the increased turbulence intensity while maintaining small integral length scales in active-grid wind tunnel flows, as the Mann model adjusts its parameters to fit the measured turbulence spectra. Similar behaviour of the Mann parameters, characterised by high $\alpha\epsilon^{2/3}$ values and integral length scales on the order of a few centimetres, has been reported in recent wind tunnel studies (Wang

https://doi.org/10.5194/egusphere-2026-825
Preprint. Discussion started: 1 June 2026


et al., 2025). This behaviour was attributed to the turbulent boundary layer not being fully developed, which leads to evolving turbulence characteristics.

Both the Mann-based lidar spectra and the measured lidar spectra exhibit the expected attenuation relative to the hot-wire spectra due to probe averaging effect. However, for configuration IV with $l_{\mathrm{p}} = 0.34\,\mathrm{m}$, a noticeable discrepancy remains between the measured and Mann-based lidar spectra. This discrepancy may partly due to the higher spectral energy at low wave numbers in the modelled hot-wire spectrum used as input for the lidar spectral modelling, as well as possible misalignment between the lidar beam and the mean flow direction.

In Figure 12, a few variance ratios obtained from the maximum method are greater than 1 which contradicts the theory of filtered lidar measurements and can likely be attributed to inhomogeneities in the flow. These inhomogeneities may be caused by a velocity gradient or by measurement noise along the lidar probe volume. In the same figure, from three conventional methods, the maximum method has the least underestimation, which is in agreement with previous findings (Held and Mann, 2018).

We described the post-processing sequence of the Doppler lidar spectra and demonstrated that accurate removal of the noise spectrum is a critical step for spectrum-based lidar variance estimation. In particular, the choice of the noise threshold can have a substantial impact when the Doppler spectrum exhibits asymmetric distribution tails as observed in this study, because the second-order moment of the averaged spectrum i.e. the variance is highly sensitive to the PDF tails. Therefore, a more conservative noise threshold of $\mu_{\mathrm{noise}} + 3\sigma_{\mathrm{noise}}$ was used in this study. However, except for cases with pronounced tail-like PDFs, and especially when the spectral signal exhibits a low CNR, as is often the case in field measurements, the use of the minimum feasible noise threshold (i.e. $\mu_{\mathrm{noise}}$) is recommended to preserve the main spectral peak.

We showed that neither noise threshold nor area normalization of the lidar spectra explain the overestimation of spectrum-based variances in this study, although both factors do influence variance estimation. The consistent overestimation of the spectrum-based lidar variance estimation arises from the broader width of the averaged lidar spectrum PDF, which suggests that the flow within the probe volume is not statistically homogeneous. Variations observed in the individual spectra confirm that this effect is due to the flow itself. For instance, in Fig. 14c while the dominant velocity is approximately 7.5 m $\mathrm{s}^{-1}$, all lidar spectra for this case exhibit velocity distribution around to 5.5 m $\mathrm{s}^{-1}$ contrary to the hot-wire PDF, producing a tail-like distribution and thereby broadening the spectrum width and increasing the variance estimation. The presence of these additional velocity components in several cases may be attributed to several factors: the flow being not yet fully developed along the tunnel and within the probe volume, i.e., velocity gradients, slight misalignment of the laser beam with the flow direction, which could result in sampling different flow structures than those captured by the hot wire, or the close proximity of the measurement location to the hot-wire structure (5 cm), which may induce flow deflection around the structure and create velocity variations within the lidar probe volume. Among the possible causes, the effect of velocity gradients along the probe volume was explicitly analysed. The gradient was estimated from the velocity difference between two reference hot-wire measurements along the tunnel, assuming a linear variation along the distance. A similar linear interpolation approach was applied to VAD measurements at different heights to account for vertical shear, and the resulting effect was corrected (Mann

https://doi.org/10.5194/egusphere-2026-825
Preprint. Discussion started: 1 June 2026


et al., 2010). Nevertheless, it is not always possible to detect or correct for all velocity gradients within the probe volume, particularly for scan trajectories influenced by wake flows in the open field.

Although very successful, the settings of the active grid and the CW lidar impose a number of limitations. Various turbulence intensity levels and integral length scales were generated using the active grid in the wind tunnel; however, the resulting spectra do not necessarily replicate those observed in atmospheric flows. Measurements were performed at two hot-wire locations, with the lidar focus adjusted for each measurement; in other words, we have repetitive hot-wire measurements at the same measurement locations. The main reason for the differences in flow at the same hot-wire measurement location is probably due to differences in the free-stream temperature, which resulted in slight differences in the flow properties despite the same protocol being used. The flow is not fully-developed along the tunnel, as evidenced by the increase in mean velocity at the second measurement point further downstream. This indicates the presence of a velocity gradient along the tunnel. Moreover, TI is higher at measurement location closer to the grid, at the 1.5 m downstream position (configurations II and IV), which indicates higher fluctuations at these points. Because the spectrum-based lidar variance estimation method is highly sensitive to velocity gradients and fluctuations within the probe volume, these effects can lead to an overestimation of the lidar-derived variance. To quantify this behaviour, the ratio of spectrum-based lidar variance to hot-wire variance is examined as a function of measurement configurations and grid protocols. As shown in Fig. 15, the spectrum-based variance overestimation is consistently higher for configurations II and IV, with the largest overestimation occurring in configuration IV, where the probe volume is largest. These results indicate that spectrum-based lidar variance estimates are strongly influenced by flow inhomogeneity within the probe volume. Consequently, improved agreement between spectrum-based lidar variance estimates and reference measurements is expected when the flow is homogeneous within the probe volume, such as in 10-min statistics of atmospheric open field conditions. In contrast, similar overestimations may arise in flows characterized by strong inhomogeneity, for example within the wake of a wind turbine.

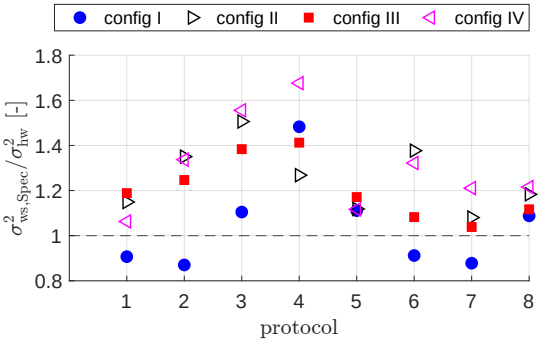


**Figure 15.** Ratio of the spectrum-based lidar variance to the hot-wire variance for varying configurations and active grid protocols. The dashed line indicates the ideal value of 1.

For future wind tunnel studies using lidar measurements, it is suggested that the flow characteristics and possible sensor interferences within the probe volume are analysed by preliminary tests. Similarly, for studies aiming to model turbulent spectra

https://doi.org/10.5194/egusphere-2026-825
Preprint. Discussion started: 1 June 2026


using active grids, careful consideration should be given to the selection of grid protocols to ensure a realistic representation of the target spectral characteristics.

## 7 Conclusions

We investigated the effect of probe volume averaging on the along-wind turbulence characteristics measured with a CW lidar in a wind tunnel. Using the tunnel's active grid, flows with a range of turbulence intensities and integral length scales were generated, while varying the lidar location and focus distance to produce four different probe volumes. This setup enabled, for the first time, an experimental investigation using 32 distinct probe volume over integral length scale ratios ranging from 0.08 to 8.85 which are representative of open field lidar measurement ratios.

We modelled the probe volume averaging in the lidar spectra by applying a theoretical lidar filter function to the Mann model of the hot-wire data. Lidar measurement noise is evident from the increase in spectral energy at higher wave numbers (>10 $m^{-1}$) across all cases. Apart from this noise region, the modelled lidar spectra exhibited the expected attenuation relative to the hot-wire spectra due to probe volume averaging. However, the accuracy of the lidar spectra model strongly depends on the accuracy of the modelled hot-wire spectra used as input. Any discrepancies between the modelled and measured hot-wire spectra propagate through the filter function, leading to corresponding discrepancies in the modelled lidar spectra. Additionally, slight misalignments between the lidar beam and the incoming flow, varying by a few degrees, can further contribute to these differences. Despite these discrepancies, both the modelled and measured spectra captured the expected decrease in the ratio of lidar to hot-wire spectra with increasing probe volume across all studied cases.

We also demonstrated that the measured and modelled lidar-based turbulence statistics, including integral length scale and variance, are highly dependent on the probe volume to integral length scale ratio, which is the primary parameter representing probe volume averaging. The lidar-derived integral length scales are significantly overestimated, ranging from 6 % to 100 % compared to the reference measurements, as probe volume averaging increases. The lidar to hot-wire variance ratios obtained from conventional methods, using only the dominant frequency of the backscattered lidar signal, drop sharply once the probe volume over integral length scale ratio exceeds 0.2. The relative error of the lidar-derived variance obtained using conventional methods increases from 10 % up to 80 % at the largest probe volume to integral length scale ratio of 8.85. This is particularly important for highly stratified conditions (e.g. stable) with small dominant turbulence structures in open field applications. However, this can become noticeable already at neutral regimes if larger probe volume lengths are used, which are associated with longer focus lengths of a few hundreds of metres.

For the first time, we experimentally estimated spectrum-based lidar variance from the averaged lidar Doppler spectrum as a function of the probe volume over integral length scale ratios. The results indicate that spectrum-based variances are range from -15 % to +70 % but largely independent of this ratio, unlike conventional variance estimation methods, and show better agreement with reference hot-wire values with an average relative error +20 %.

Since the spectrum-based lidar variance estimation method is highly sensitive to velocity gradients and fluctuations within the probe volume, these effects can contribute to an overestimation of the spectrum-based lidar derived variance. When such

https://doi.org/10.5194/egusphere-2026-825
Preprint. Discussion started: 1 June 2026


velocity gradients are estimated, as demonstrated in this study, the overestimation can be corrected, reducing the average relative error to +10 %. Despite the presence of flow gradients in the tunnel, the spectrum-based lidar variance estimation method compensates for probe volume averaging and improves the agreement with reference values demonstrating its capability for lidar-based along-wind variance estimation in both laboratory and field environments.

*Data availability.* The data used for the analysis in this paper can be made available on request.

https://doi.org/10.5194/egusphere-2026-825
Preprint. Discussion started: 1 June 2026


## Appendix A: Flow characteristics for all studied cases

**Table A1.** Setup and flow details of all measurement cases.

| Configuration | Protocol | $\bar{u}_{\mathrm{hw}}$ | $\mathrm{TI}_{\mathrm{hw}}$ | $L_{\mathrm{hw}}$ | $l_{\mathrm{p}}$ | $l_{\mathrm{p}}/L$ |
|---|---|---|---|---|---|---|
| I | 1 | 8.18 | 4.75 | 0.10 | 0.14 | 1.40 |
| I | 2 | 8.35 | 4.13 | 0.08 | 0.14 | 1.69 |
| I | 3 | 8.24 | 3.55 | 0.07 | 0.14 | 1.99 |
| I | 4 | 7.87 | 3.07 | 0.06 | 0.14 | 2.40 |
| I | 5 | 7.83 | 8.64 | 0.48 | 0.14 | 0.30 |
| I | 6 | 7.97 | 10.27 | 1.16 | 0.14 | 0.12 |
| I | 7 | 7.94 | 10.88 | 1.74 | 0.14 | 0.08 |
| I | 8 | 7.84 | 12.45 | 1.43 | 0.14 | 0.10 |
| II | 1 | 7.79 | 9.04 | 0.05 | 0.19 | 3.90 |
| II | 2 | 7.58 | 8.54 | 0.05 | 0.19 | 4.00 |
| II | 3 | 7.40 | 6.73 | 0.05 | 0.19 | 4.08 |
| II | 4 | 7.75 | 7.01 | 0.05 | 0.19 | 3.89 |
| II | 5 | 7.59 | 12.50 | 0.20 | 0.19 | 0.95 |
| II | 6 | 7.46 | 10.14 | 0.23 | 0.19 | 0.80 |
| II | 7 | 7.28 | 10.40 | 1.00 | 0.19 | 0.19 |
| II | 8 | 7.58 | 12.19 | 0.85 | 0.19 | 0.22 |
| III | 1 | 8.14 | 4.39 | 0.08 | 0.28 | 3.54 |
| III | 2 | 8.16 | 3.48 | 0.07 | 0.28 | 4.04 |
| III | 3 | 8.01 | 3.14 | 0.07 | 0.28 | 4.11 |
| III | 4 | 7.80 | 3.13 | 0.06 | 0.28 | 4.82 |
| III | 5 | 7.93 | 8.15 | 0.57 | 0.28 | 0.49 |
| III | 6 | 7.92 | 9.22 | 1.16 | 0.28 | 0.24 |
| III | 7 | 7.73 | 10.62 | 1.62 | 0.28 | 0.17 |
| III | 8 | 7.78 | 12.28 | 1.39 | 0.28 | 0.20 |
| IV | 1 | 7.80 | 9.14 | 0.05 | 0.34 | 7.16 |
| IV | 2 | 7.47 | 7.61 | 0.05 | 0.34 | 7.35 |
| IV | 3 | 7.51 | 7.01 | 0.05 | 0.34 | 7.36 |
| IV | 4 | 7.51 | 6.80 | 0.04 | 0.34 | 8.85 |
| IV | 5 | 7.48 | 11.89 | 0.22 | 0.34 | 1.57 |
| IV | 6 | 7.43 | 10.20 | 0.48 | 0.34 | 0.71 |
| IV | 7 | 7.35 | 10.90 | 1.06 | 0.34 | 0.32 |
| IV | 8 | 7.32 | 12.17 | 0.86 | 0.34 | 0.40 |

https://doi.org/10.5194/egusphere-2026-825
Preprint. Discussion started: 1 June 2026


## Appendix B: Factors influencing the estimation of spectrum-based velocity variance

### B1 Backscatter from moving objects in the measurement volume

In lidar measurements, any backscatter contributions from moving objects within the measurement field should be removed from the dataset. For example, nacelle-based lidars often experience spurious backscatter signals when turbine blades pass through the measurement volume. Similarly, in four of the present cases (configurations II & IV, protocols 5 & 6), the lidar signal was affected by the moving flaps of the active grid, located 1.5 m downstream of the lidar focus point. This resulted in Doppler radial velocity spectra with peaks around the flap velocity between -2 $\mathrm{m\,s^{-1}}$ and 2 $\mathrm{m\,s^{-1}}$ (Fig. B1). These Doppler radial velocity spectra were removed from both the lidar and hot wire dataset, which accounts for 25 % of the dataset in those cases.

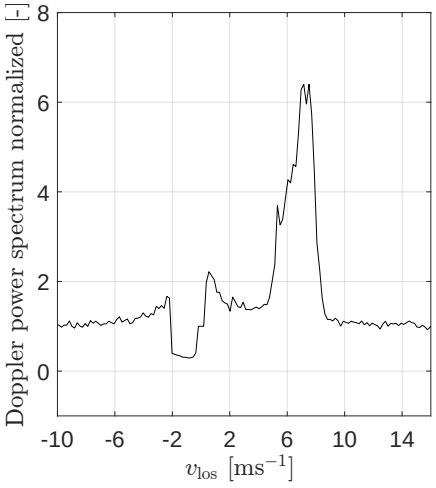


**Figure B1.** A secondary peak in the lidar Doppler spectrum around -2 $\mathrm{m\,s^{-1}}$ to 2 $\mathrm{m\,s^{-1}}$ due to the backscatter from the moving active grid flaps.

### B2 Noise threshold effect on lidar Doppler spectrum

A noise threshold, defined as the mean plus three times the standard deviation of the noise spectrum $\sigma_{\mathrm{noise}}$, was applied prior to the normalization and averaging of the radial velocity spectra. To evaluate the impact of noise removal, the threshold was systematically varied from one to five standard deviations for all cases in the dataset. The corresponding threshold limits for a representative radial velocity spectrum are illustrated in Fig. B2. Thresholds beyond five standard deviations were not tested, as higher values would clearly remove part of the signal. The resulting differences in velocity variance ratios for the five threshold definitions are shown in Fig. B1. As the standard deviation multiplier in the threshold definition increases, more of the wider part of the spectrum, including the tails is removed, leading to a reduction in the estimated variance. Consequently,

https://doi.org/10.5194/egusphere-2026-825
Preprint. Discussion started: 1 June 2026


with increasing noise threshold, the estimated variance ratio decreases relative to the one obtained with a $1\sigma_{\text{noise}}$ threshold. The mean value of the estimated variance ratios decreased from 1.37 to 1.13 as the threshold increased from $1\sigma_{\text{noise}}$ to $5\sigma_{\text{noise}}$.

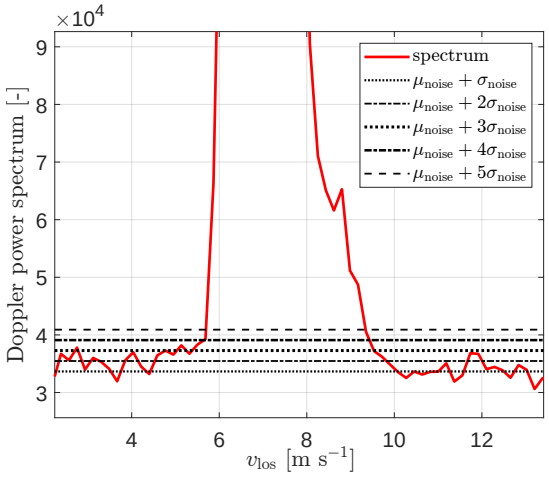


**Figure B2.** Lidar spectrum noise threshold using five different threshold definitions.

**Table B1.** Estimated variance ratios for different noise threshold definitions.

| Threshold ($\sigma_{\text{noise}}$) | Average variance ratio |
|---|---|
| 1 | 1.37 |
| 2 | 1.26 |
| 3 | 1.20 |
| 4 | 1.16 |
| 5 | 1.13 |

### B3 Normalization effect on lidar Doppler spectrum

In WindScanner measurements, the radial velocity spectrum is stored already in a normalized fashion to maintain a constant amplitude for a convenient storage. In this 'default' normalization, the peak value of the Doppler power spectrum is kept at the same level while the spectrum amplitude varies. Consequently, signals with low backscatter are characterized by lower spectral amplitudes and smaller areas, and vice versa.

Two additional normalization techniques, as described in (Branlard et al., 2013), were also applied to the data to assess their impact on the variance ratios. One technique normalizes the default spectrum using peak value amplitudes, known as 'peak normalization', ensuring that low and high backscatter signals contribute equally during ensemble averaging. The second technique, known as 'area normalization' assumes constant energy for each radial velocity spectrum so performs area normalization on the default spectrum.

https://doi.org/10.5194/egusphere-2026-825
Preprint. Discussion started: 1 June 2026


Ensemble averaging of the Doppler spectrum was performed using the default normalization method as well as two alternative normalization techniques. The resulting velocity variance ratios obtained with area normalization were nearly identical to those derived using the default approach. In contrast, the use of peak normalization led to an increase in the variance ratio by up to 0.08.

### B4 The effect of velocity gradient along the probe volume on spectrum-based lidar velocity variance estimation

This section provides an additional figure showing ratio of the spectrum-based lidar variance to the hot-wire variance after the velocity gradient correction.

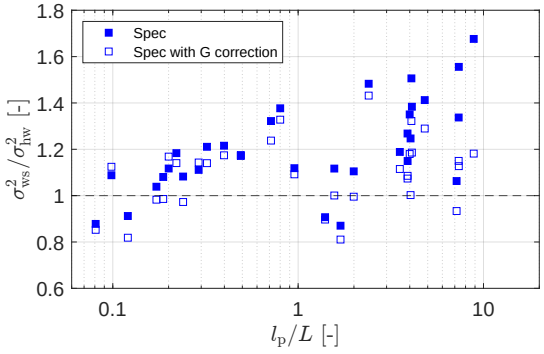


**Figure B3.** Ratio of the spectrum-based lidar variance to the hot-wire variance with and without velocity gradient G correction. The dashed line indicates the ideal value of 1.

*Author contributions.* SU designed the test matrix, performed the measurements and analysis, and wrote the paper. AP contributed with the Mann model of the measurements. AR helped interpreting the results throughout the study. MK initiated the measurement campaign, provided extensive reviews and had a supervisory role. All authors revised and edited the manuscript.

*Competing interests.* The authors declare no competing interests

*Acknowledgements.* This work was funded by the German Federal Ministry for Economic Affairs and Climate Action (grant no. 0325936H) in the scope of the DFWind Phase 2 project on the basis of a decision by the German Bundestag.

We would like to acknowledge Lars Neuhaus for providing the active grid protocols and helping set up the hot-wire system.

https://doi.org/10.5194/egusphere-2026-825
Preprint. Discussion started: 1 June 2026


## References

Angelou, N., Mann, J., Sjöholm, M., and Courtney, M.: Direct measurement of the spectral transfer function of a laser based anemometer, Review of Scientific Instruments, 83, https://doi.org/10.1063/1.3697728, 2012.

Branlard, E., Pedersen, A. T., Mann, J., Angelou, N., Fischer, A., Mikkelsen, T., Harris, M., Slinger, C., and Montes, B. F.: Retrieving wind statistics from average spectrum of continuous-wave lidar, Atmospheric Measurement Techniques, 6, 1673–1683, https://doi.org/10.5194/amt-6-1673-2013, 2013.

Brugger, P., Träumner, K., and Jung, C.: Evaluation of a Procedure to Correct Spatial Averaging in Turbulence Statistics from a Doppler Lidar by Comparing Time Series with an Ultrasonic Anemometer, Journal of Atmospheric and Oceanic Technology, 33, 2135 – 2144, https://doi.org/10.1175/JTECH-D-15-0136.1, 2016.

Cheynet, E., Jakobsen, J. B., Snæbjörnsson, J., Mann, J., Courtney, M., Lea, G., and Svardal, B.: Measurements of Surface-Layer Turbulence in a Wide Norwegian Fjord Using Synchronized Long-Range Doppler Wind Lidars, Remote Sensing, 9, https://doi.org/10.3390/rs9100977, 2017.

Conti, D., Dimitrov, N., Peña, A., and Herges, T.: Probabilistic estimation of the Dynamic Wake Meandering model parameters using SpinnerLidar-derived wake characteristics, Wind Energy Science, 6, 1117–1142, https://doi.org/10.5194/wes-6-1117-2021, 2021.

Dellwik, E., Sjöholm, M., and Mann, J.: An evaluation of the WindEye wind lidar, Tech. Rep. 0078, DTU Wind Energy, https://orbit.dtu.dk/en/publications/an-evaluation-of-the-windeye-wind-lidar/, 2015.

Drobinski, P., Dabas, A. M., and Flamant, P. H.: Remote Measurement of Turbulent Wind Spectra by Heterodyne DopplerLidar Technique, Journal of Applied Meteorology, 39, 2434 – 2451, https://doi.org/10.1175/1520-0450(2000)039<2434:RMOTWS>2.0.CO;2, 2000.

Frehlich, R.: Effects of Wind Turbulence on Coherent Doppler Lidar Performance, Journal of Atmospheric and Oceanic Technology, 14, 54 – 75, https://doi.org/10.1175/1520-0426(1997)014<0054:EOWTOC>2.0.CO;2, 1997.

Frehlich, R., Hannon, S. M., and Henderson, S. W.: Coherent Doppler Lidar Measurements of Wind Field Statistics, Boundary-Layer Meteorology, 86, 233–256, https://doi.org/10.1023/A:1000676021745, 1998.

Frehlich, R., Meillier, Y., and Jensen, M. L.: Measurements of Boundary Layer Profiles with In Situ Sensors and Doppler Lidar, Journal of Atmospheric and Oceanic Technology, 25, 1328 – 1340, https://doi.org/10.1175/2007JTECHA963.1, 2008.

Fu, W., Peña, A., and Mann, J.: Turbulence statistics from three different nacelle lidars, Wind Energy Science, 7, 831–848, https://doi.org/10.5194/wes-7-831-2022, 2022.

Fu, W., Sebastiani, A., Peña, A., and Mann, J.: Dependence of turbulence estimations on nacelle lidar scanning strategies, Wind Energy Science, 8, 677–690, https://doi.org/10.5194/wes-8-677-2023, 2023.

Held, D. P. and Mann, J.: Comparison of methods to derive radial wind speed from a continuous-wave coherent lidar Doppler spectrum, Atmospheric Measurement Techniques, 11, 6339–6350, https://doi.org/10.5194/amt-11-6339-2018, 2018.

Knoop, S., Bosveld, F. C., Haij, M. J. D., and Apituley, A.: A 2-year intercomparison of continuous-wave focusing wind lidar and tall mast wind measurements at Cabauw, Atmospheric Measurement Techniques, 14, 2219–2235, https://doi.org/10.5194/amt-14-2219-2021, 2021.

Kröger, L., Frederik, J., van Wingerden, J.-W., Peinke, J., and Hölling, M.: Generation of user defined turbulent inflow conditions by an active grid for validation experiments, Journal of Physics: Conference Series, 1037, 52 002, https://doi.org/10.1088/1742-6596/1037/5/052002, 2018.

Liu, Z., Barlow, J. F., Chan, P.-W., Fung, J. C. H., Li, Y., Ren, C., Mak, H. W. L., and Ng, E.: A Review of Progress and Applications of Pulsed Doppler Wind LiDARs, Remote Sensing, 11, https://doi.org/10.3390/rs11212522, 2019.

https://doi.org/10.5194/egusphere-2026-825
Preprint. Discussion started: 1 June 2026


Manami, M., Mann, J., Sjöholm, M., Léa, G., and Gorju, G.: Squeezing turbulence statistics out of a pulsed Doppler lidar, Atmospheric Measurement Techniques, 18, 7513–7523, https://doi.org/10.5194/amt-18-7513-2025, 2025.

Mann, J.: The spatial structure of neutral atmospheric surface-layer turbulence, Journal of fluid mechanics, 273, 141–168, 1994.

Mann, J., Cariou, J.-P. C., Parmentier, R. M., Wagner, R., Lindelöw, P., Sjöholm, M., and Enevoldsen, K.: Comparison of 3D turbulence measurements using three staring wind lidars and a sonic anemometer, Meteorologische Zeitschrift, 18, 135–140, https://doi.org/10.1127/0941-2948/2009/0370, 2009.

Mann, J., Peña, A., Bingöl, F., Wagner, R., and Courtney, M. S.: Lidar Scanning of Momentum Flux in and above the Atmospheric Surface Layer, Journal of Atmospheric and Oceanic Technology, 27, 959 – 976, https://doi.org/10.1175/2010JTECHA1389.1, 2010.

McWilliams, J. C., Meneveau, C., Patton, E. G., and Sullivan, P. P.: Stable Boundary Layers and Subfilter-Scale Motions, Atmosphere, 14, https://doi.org/10.3390/atmos14071107, 2023.

Mikkelsen, T.: Lidar-based Research and Innovation at DTU Wind Energy – a Review, Journal of Physics: Conference Series, 524, 12 007, https://doi.org/10.1088/1742-6596/524/1/012007, 2014.

Mikkelsen, T., Angelou, N., Hansen, K., Sjöholm, M., Harris, M., Slinger, C., Hadley, P., Scullion, R., Ellis, G., and Vives, G.: A spinner-integrated wind lidar for enhanced wind turbine control, Wind Energy, 16, 625–643, https://doi.org/10.1002/we.1564, 2013.

Nandi, T. N. and Yeo, D. H.: Estimation of integral length scales across the neutral atmospheric boundary layer depth: A Large Eddy Simulation study, Journal of Wind Engineering and Industrial Aerodynamics, 218, 104 715, https://doi.org/10.1016/j.jweia.2021.104715, 2021.

Neuhaus, L., Berger, F., Peinke, J., and Hölling, M.: Exploring the capabilities of active grids, Experiments in Fluids, 62, 130, https://doi.org/10.1007/s00348-021-03224-5, 2021.

Pedersen, A. T. and Courtney, M.: Flywheel calibration of a continuous-wave coherent Doppler wind lidar, Atmospheric Measurement Techniques, 14, 889–903, https://doi.org/10.5194/amt-14-889-2021, 2021.

Peña, A.: Østerild: A natural laboratory for atmospheric turbulence, Journal of Renewable and Sustainable Energy, 11, 063 302, 2019.

Peña, A. and Mann, J.: Turbulence Measurements with Dual-Doppler Scanning Lidars, Remote Sensing, 11, https://doi.org/10.3390/rs11202444, 2019.

Peña, A., Mann, J., and Dimitrov, N.: Turbulence characterization from a forward-looking nacelle lidar, Wind Energy Science, 2, 133–152, https://doi.org/10.5194/wes-2-133-2017, 2017.

Peña, A., Yankova, G. G., and Mallini, V.: On the lidar-turbulence paradox and possible countermeasures, Wind Energy Science, 10, 83–102, https://doi.org/10.5194/wes-10-83-2025, 2025.

Puccioni, M. and Iungo, G. V.: Spectral correction of turbulent energy damping on wind lidar measurements due to spatial averaging, Atmospheric Measurement Techniques, 14, 1457–1474, https://doi.org/10.5194/amt-14-1457-2021, 2021.

Sathe, A., Mann, J., Gottschall, J., and Courtney, M. S.: Can Wind Lidars Measure Turbulence?, Journal of Atmospheric and Oceanic Technology, 28, 853 – 868, https://doi.org/10.1175/JTECH-D-10-05004.1, 2011.

Schottler, J., Reinke, N., Hölling, A., Whale, J., Peinke, J., and Hölling, M.: On the impact of non-Gaussian wind statistics on wind turbines – an experimental approach, Wind Energy Science, 2, 1–13, https://doi.org/10.5194/wes-2-1-2017, 2017.

Sekar, A. P. K., Hulsman, P., Dooren, M. F. V., and Kühn, M.: Synchronised WindScanner field measurements of the induction zone between two closely spaced wind turbines, Wind Energy Science, 9, 1483–1505, https://doi.org/10.5194/wes-9-1483-2024, 2024.

Siegman, A. E.: Lasers, University science books: Mill Valley, CA,, 1986.

https://doi.org/10.5194/egusphere-2026-825
Preprint. Discussion started: 1 June 2026


Sjöholm, M., Mikkelsen, T., Mann, J., Enevoldsen, K., and Courtney, M.: Spatial averaging-effects on turbulence measured by a continuous-wave coherent lidar, Meteorologische Zeitschrift, 18, 281–287, https://doi.org/10.1127/0941-2948/2009/0379, 2009.

Sonnenschein, C. M. and Horrigan, F. A.: Signal-to-Noise Relationships for Coaxial Systems that Heterodyne Backscatter from the Atmosphere, Appl. Opt., 10, 1600–1604, https://doi.org/10.1364/AO.10.001600, 1971.

Uluocak, S., Theuer, F., Neuhaus, L., Inestroza, M. A. Z., Hulsman, P., and Kühn, M.: The lidar probe volume averaging effect: A wind tunnel investigation in streamwise turbulence with continuous-wave lidar, Journal of Physics: Conference Series, 2767, 42 027, https://doi.org/10.1088/1742-6596/2767/4/042027, 2024.

van Dooren, M. F., Sekar, A. P. K., Neuhaus, L., Mikkelsen, T., Hölling, M., and Kühn, M.: Modelling the spectral shape of continuous-wave lidar measurements in a turbulent wind tunnel, Atmospheric Measurement Techniques, 15, 1355–1372, https://doi.org/10.5194/amt-15-1355-2022, 2022.

Wang, X., Liu, H., Li, M., Mann, J., and Li, S.: Turbulence structure in a boundary layer wind tunnel, Physics of Fluids, 37, https://doi.org/10.1063/5.0246592, 2025.

Zhou, B., Li, Y., and Zhu, K.: Improved Length Scales for Turbulence Kinetic Energy–Based Planetary Boundary Layer Scheme for the Convective Atmospheric Boundary Layer, Journal of the Atmospheric Sciences, 77, 2605–2626, https://doi.org/10.1175/JAS-D-19-0334.1, 2020.